NOVEL BROADBAND TERAHERTZ NEGATIVE REFRACTIVE INDEX METAMATERIALS: ANALYSIS AND EXPERIMENT

N. Wongkasem and A. Akyurtlu

Department of Electrical and Computer Engineering
University of Massachusetts, Lowell
Lowell, MA 01854, USA

J. Li, A. Tibolt, Z. Kang, and W. D. Goodhue

Department of Physics and Applied Physics
University of Massachusetts, Lowell
Lowell, MA 01854, USA

Abstract—Broadband planar and non-planar negative refractive index (NRI) metamaterial (MTM) designs consisting of a periodically arranged split ring resonator and wire structures are developed in the terahertz (THz) frequency regime using the Finite-Difference Time-Domain (FDTD) method. The novel MTM designs generate a broad negative index of refraction (NIR) passband approximately two and a half times higher than those of the conventional SRR/wire structures, by using the same dimensions. Numerical simulations of wedge- and triangle-shaped metamaterials are used to prove the negative refractive index of the models. The fabricated MTMs exhibit passband characteristics which are in good agreement with the model results. The parametric studies of correlated factors further support these outcomes.

1. INTRODUCTION

Materials that support strong, tunable magnetic and electric properties in the THz frequency range have applications in personnel security screening, medical imaging, remote sensing, and bio-medical engineering [1–3]. THz radiation has the ability to show polarization sensitivity. It is also able to see through common materials, such as clothing, thick smoke and dust [1] so that it can detect concealed

weapons since many non-metallic, non-polar materials are transparent to THz radiation [2]. When assembling the metamaterials (MTM) at THz or higher frequencies by scaling down the dimensions of the resonators, the major inconvenience we face is the difficulty of the small-scale manufacturing process.

We propose and demonstrate a model of spilt-ring resonator/wire composite MTM which can create a negative index passband approximately two and a half times higher than those of the conventional SRR/wire structures, with identical dimensions. The magnetic field is excited parallel to the plane of the structure, so that the propagation direction is normal to the plane and the electric field is parallel to the gap-side of the SRR. This higher passband results in doubling up the size of the conventional structure in order to get the same location of the transmission band. Increasing the size of the structure will significantly simplify the nanofabrication when we deal with MTMs in the optical regime. Furthermore, the new SRR/wire structure can produce a broad passband - nearly two and a half times larger than those of the primary models. One design has been fabricated by using aluminum (Al) on a Mylar substrate using a combination of standard lift-off and photolithographic techniques. The transmission spectra of this group of samples are measured using Fourier transform infrared (FT-IR) interferometer and the results are compared to those of the simulation model. Parametric studies of the different factors of the simulation and experimental models such as thickness, materials, and misalignment are also discussed.

2. ANALYSIS

Four different cases of SRRs, as defined by Katsarakis et al. are employed. The magnetic field is oriented perpendicular to the SRR plane for cases (a) and (b), henceforth referred to as SRR-A and SRR-B respectively, and it is in the SRR plane for cases (c) and (d), henceforth referred to as SRR-C and SRR-D, respectively. The electric field for SRR-B and SRR-D structures is along the gap-bearing sides of the SRR, whereas for SRR-A and SRR-C, is along the no-gap side of the SRR structures [4]. The direction of propagation is along the SRR structures for SRR-A and SRR-B, and is perpendicular to the structures for SRR-C and SRR-D. The outer, inner, and double-ring of the SRR cases A-D are shown in Fig. 1.

Besides the conventional cases [5] (SRR-A and SRR-B), it has been shown that the SRR-D configuration, where the EM waves propagate perpendicular to the plane and the electric field is along the gap side, can also generate a magnetic response [4, 6–8], Ref. [7] assesses
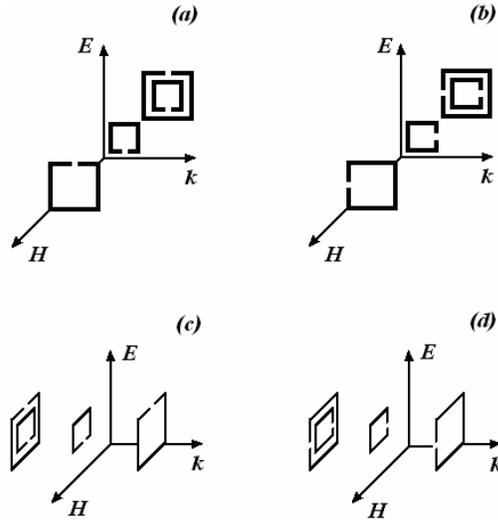
Figure 1. Field and direction of propagation orientation of double, inner, and outer split ring resonator (back to front) of (a) SRR-A, (b) SRR-B (left to right), (c) SRR-C, (d) SRR-D.

the magnetoelectric coupling in the structure to complete the formal model of Ref. [5] which considered the magnetic polarizability only. Nevertheless, all four resonant polarizabilities, magnetic, electric and two magnetoelectric should come about as a result of the structure physics [7]. Hence, it can be concluded that not only the magnetic polarizability has an effect on the SRR-A and SRR-B structures, but the electric and magnetoelectric polarizabilities also cause resonance for the SRR-B and SRR-D structures. As we will show later, a resonance of the SRR-C, which appears in a higher frequency, can be caused by one or more polarizabilities.

By adjusting the geometric parameters, including linewidth, width, length, thickness, and gap distance of the SRR structures, the resonance can be tuned to a specific frequency of interest [5]. The dimensions of the SRR structures are $93.6\,\mu$m by $93.6\,\mu$m. The outer square SRR side length is $93.6\,\mu$m, the inner square SRR side length is $62.4\,\mu$m, and the distance between the inner and outer SRR is $7.8\,\mu$m. Each line width is $7.8\,\mu$m and the gap is $15.6\,\mu$m. Fig. 2(a)–(d) shows the simulated transmission spectra of the double, outer, and inner ring SRR of SRR cases (a), (b), (c), and (d), respectively. These simulations were obtained using a FDTD model with periodic boundary conditions [9, 10]. The first resonance of the double ring occurs around $350\,$GHz
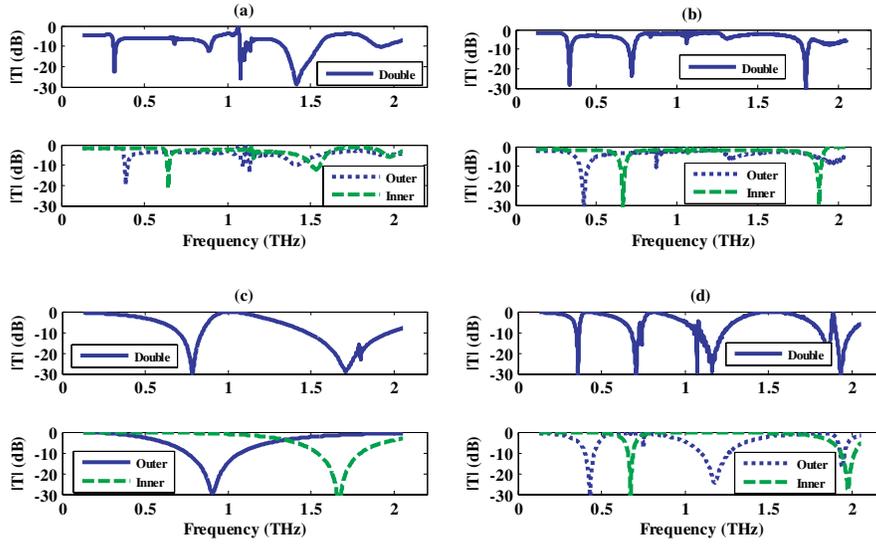
Figure 2. Simulated transmission spectra of double (top-solid line), outer (bottom-dotted line), and inner (bottom-dashed line) of the four orientations (a) SRR-A, (b) SRR-B, (c) SRR-C, and (d) SRR-D.

for cases (a), (b) and (d). However, the first resonance occurs at a much higher frequency, 800 GHz, in case (c).

The first resonance of all four cases of the SRR configurations is the magnetic response of the outer ring while the second resonance corresponds to the resonance of the inner ring. The shifts between the resonances of the double-ring and the outer and inner ring are due to the additional capacitance between the rings [11]. The interesting result is obtained in SRR-C, where the outer and inner rings generate resonances at 820 and 1,650 GHz, respectively, as illustrated in Fig. 2(c). Consequently, the double-ring SRR-C has the first and the second resonance at 800 GHz and 1,660 GHz respectively. Although numerical and experimental results [4, 7, 8, 12] have shown that there is no resonance in the SRR-C at the same frequency as those of the other SRRs, the results do not cover a higher frequency where the resonances of each individual ring (inner and outer) occur. The SRR-C is in essence the SRR-A case with a 90° rotation of the SRR plane while its axis is fixed. In fact, SRR-A and SRR-C have the same configuration, but a different angle of incidence. The SRR-A (incident angle = 0°) starts to have a second dip when the incident angle increases. The second dip will become the main

resonance when the angle is close to 90° [13, 14]. Eventually, there will be a forbidden band at a higher frequency and the first resonance will disappear in the SRR-C (incident angle = 90°). Note that the structure needs to be symmetric to avoid the magnetoelectric polarizabilities. This phenomenon can be explained by polarization conversion which corresponds to a transmission change [15–17]. This higher-order magnetic resonance, marked as a magnetic-dipole mode, is also identified in a single ring [14].

Another important factor to consider in the analysis of the SRR-C structure is the interaction of the inclusions with their neighboring structures within the array. Here, we analyze and compare the response of the four types of SRRs under a transverse electromagnetic mode (TEM), the most suitable mode for a semi-infinite and a finite model. The semi-infinite and finite models are implemented by PEC (perfect electric conductor) — PMC (perfect magnetic conductor) and PEC — PML (perfectly matched layer) boundary conditions, respectively. The PEC is in the direction of the electric field while PMC and PML are in the direction of the magnetic field. A comparison of the semi-infinite layer and the finite cases, namely one, five and ten layers in the direction perpendicular to the direction of propagation is shown in Fig. 3. The magnetic resonances of all types of the SRR structures become stronger when the number of SRRs increases according to the coupling between the neighboring SRRs as illustrated in Fig. 3(a)–(d). It is true for all SRR types that finite number of structures, e.g., 10 (with a proper geometric arrangement [8]) are enough to show the resonances This also proves that the resonance of SRR-C does not occur by chance, but as a result of the higher-order magnetic-dipole mode, as mentioned before, and the coupling between their neighboring elements.

When the electric field is parallel to the "no gap" sides of the SRR-C, its polarization will be symmetric and the polarization current is only flowing up and down the sides of the SRR, as shown in [4]. Conversely, for the SRR-D, the current flows between the sides compliant with the broken symmetry. The circulating current inside the SRR couples with the magnetic resonance. However, presuming the gap is very small, there can be a circulating current inside the SRR-C as well. Here, we consider only the outer-ring, as its magnetic response dominates the SRR [11]. The gap of the outer ring is varied from $15.6\,\mu$m up to the size of the (inner) ring side ($78\,\mu$m). Results in Fig. 4 show that when the gap is broad, the resonance location shifts upward. For this reason, we may conclude that the resonance of SRR-C is not related to the electric coupling.
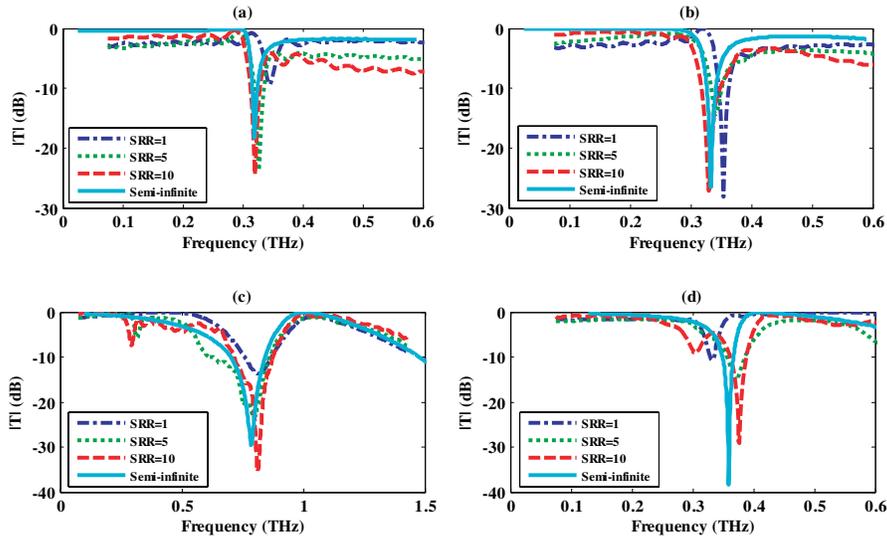
Figure 3. Simulated transmission spectra of the individual SRR (dash-dot line), five (dotted-line), ten (dashed-line) and semi-infinite (solid-line) SRRs of (a) SRR-A, (b) SRR-B, (c) SRR-C, and (d) SRR-D.
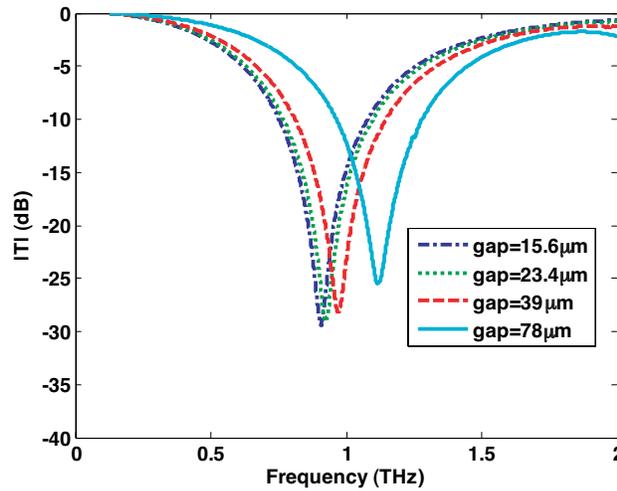

Figure 4. Simulated transmission spectra of the outer SRR-C with a 15.6 μm (dash-dot line), 23.4 μm (dotted-line), 39.0 μm (dashed-line) and 78.0 μm (solid-line) gap.
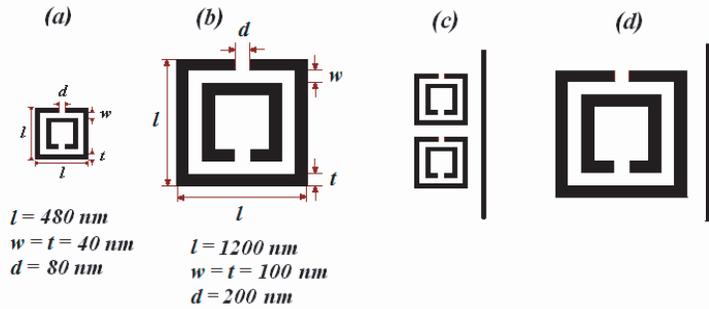
Figure 5. Dimensions of (a) SRR-A, SRR-B, and SRR-D and (b) SRR-C. Planar orientation of MTM composed of (c) SRR-A, SRR-B, and SRR-D and (d) SRR-C.

3. DESIGN AND NUMERICAL RESULTS

We will discuss the NIR passband of the planar metamaterials constructed by SRR-A, SRR-B, SRR-C and SRR-D, and an array of discontinuous wires [18]. The dimension of the SRR-A, SRR-B, and SRR-C is 480 nm by 480 nm. The outer square SRR side length is 480 nm, the inner square SRR side length is 320 nm and the distance between the inner and outer SRR is 40 nm. Every line width is 40 nm while the gap is 80 nm. The size of the SRR-C is two and a half more than that of the other SRRs, as shown in Figs. 5(a) and (b). The arrays of wires with the width and the thickness both 40 nm and 100 nm are modeled to provide the stop bands for the MTM cases a, b and d, and MTM case c for the lengths of 1380 nm, and 1400 nm respectively. Consequently, two SRR structures are combined with the wires to form the composite MTM cases a, b, and d and the 1400 nm-long wires are combined with a SRR-C to produce the passband at 50 THz as illustrated in Figs. 5(c) and (d).The transmission spectra of the MTM composed of SRR cases a–d are shown in Fig. 6. The aforementioned dimensions are designed to produce the NIR pass band in the range of 45 to 75 THz. All four planar MTMs are able to generate the NIR transmission peaks at the desired frequency. The band widths of the MTM cases a, b, and d are about 10 THz, while that composed of SRR-C is approximately 25 THz. The MTM case c has a better quality pass band (0 dB). Those of the other cases are roughly at −12 to −16 dB.

It is known that a peak of the wire/SRR is truly left-handed if the peak is located in between or above the magnetic resonance frequency (of SRRs) and below the plasma frequency (of wires) of the
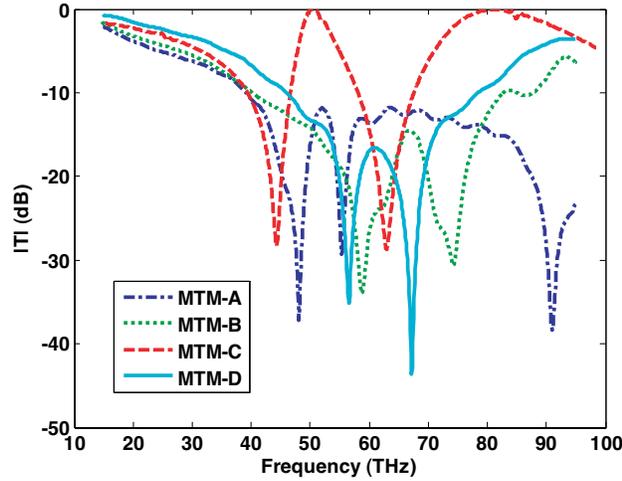
Figure 6. Simulated transmission spectra of the MTM case a (dash-dot line), case b (dotted-line), case c (dashed-line) and case d (solid-line) gap.

wire/SRR [19, 20] shown in the Figs. 9(a) and (b). Besides this, we can also identify a negative index property of the peak by using the Snell's law experiment on a wedge-shaped structure [21], one of the most intuitive verifications of negative index materials (NIM), for the parallel propagation. In case of a perpendicular propagation, when the structure form may be interpreted as electromagnetic crystal (EC), an oblique incident is required to verify the negative index of refraction.

We propose the triangle-shaped structure which can also employ the excitation in different angles. Propagation directions of the NIM in a 22° Wedge- and 22°–22° Triangle-shaped models are shown in Figs. 7(a)–(b) and (c)–(d), respectively. The base and the height of the wedge model have six and three sets of MTM-C, respectively. The number of MTM-C decreases by two in a consecutive row to construct the 22 degree angle. Each SRR-C in each MTM-C has the same dimensions as discussed before in the analysis section. The wire with $119.2\,\mu$m length has the same linewidth as that of the SRR. The spacing between each linewidth (SRR and wire) is $7.8\,\mu$m. These dimensions are also used in the fabrication technique and testing section. According to the perfect magnetic conductor (PMC) set up on the top and bottom, only one layer of the MTMs on the direction of propagation is required. The other two sides where the MTMs are placed have perfect electric conductor (PEC) boundaries.
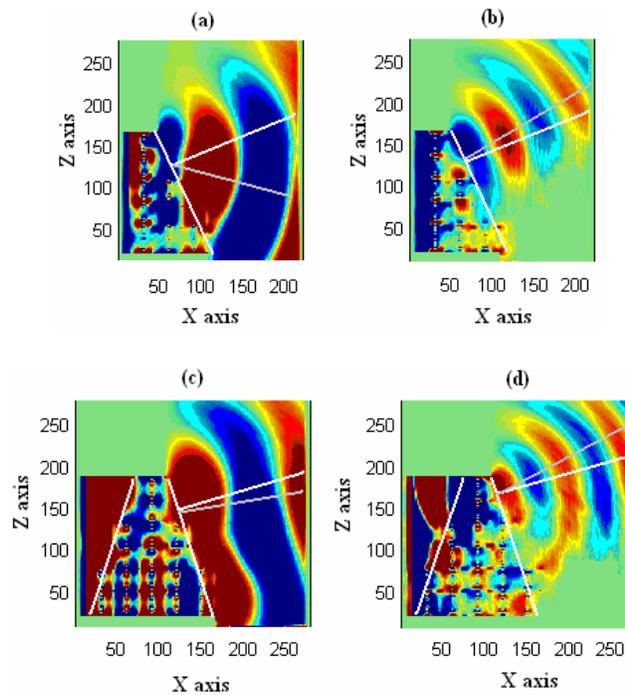
Figure 7. Propagation directions in Wedge- and Triangle-shaped models: (a) Wedge model with positive index at 600 GHz, (b) Wedge model with negative index at 900 GHz, (c) Triangle model with positive index at 600 GHz, (d) Triangle model with negative index at 950 GHz.

The remaining boundaries are set by using a perfectly matched layer (PML) boundary condition to absorb the radiated fields. The similar arrangement is set for the isosceles triangle model with 68 degrees for the bases. Figs. 7(a) and (c) illustrate the positive index of the structure in Fig. 8 at 600 GHz while the NIR shown at 900, and 950 GHz in Figs. 7(b) and (d), which is the region where NIR behavior is expected.

4. FABRICATION TECHNIQUE AND TESTING

The non-planar composite metamaterial composed of the SRR-C and wire configuration is fabricated using standard lift-off and photolithography techniques on a 50 μm thick Mylar substrate. The electric field is aligned along the wires and the direction of wave
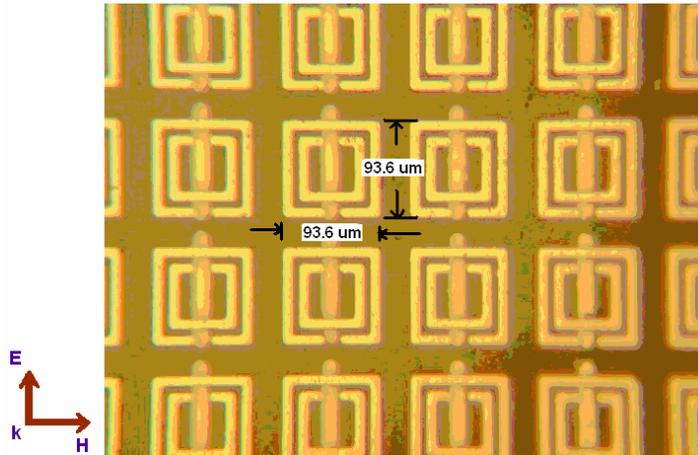
Figure 8. Photograph of the SRR/wire sample.

propagation is perpendicular to the structures, because this case is easier to align and eliminates the need to fabricate multiple layers. Each sample has SRR patterns on one side of the sheet and either a wire pattern or no pattern on the other side. The SRR and wire patterns are made of aluminum with the thickness ranging from 0.1 to 0.4 μm. The dimensions of the samples are 1.5 cm by 2 cm or approximately 20,000 unit cells. Using an FT-IR interferometer, we measure the transmission spectra of the samples. A photograph of the SRR/wire sample is shown in Fig. 8.

Fig. 9(a) shows the measured transmission spectra of the array of SRR-only and the MTM composite sample, respectively. The NIR transmission band centered at 800 GHz is at about −12 dB with 250 GHz width compared to the simulation result in Fig. 9(b) which has the pass band at 820 GHz at −20 dB with 300 GHz width. The results in Fig. 9(b) were generated through simulation of the transmission spectra of the non-planar SRR-C with the above-mentioned dimension and the wire structure of 109.2 μm.

The simulation results correctly predict the resonance frequencies, as well as the shape of the transmission spectra. Some discrepancies appear between the experimental and numerical results. In the numerical simulations, the transmission band appears at a higher frequency than in the experimental results and also has a wider passband. Furthermore, the transmission value of the simulations is lower than the experimental one. There are several factors that contribute to the differences in results. First, the thickness of the
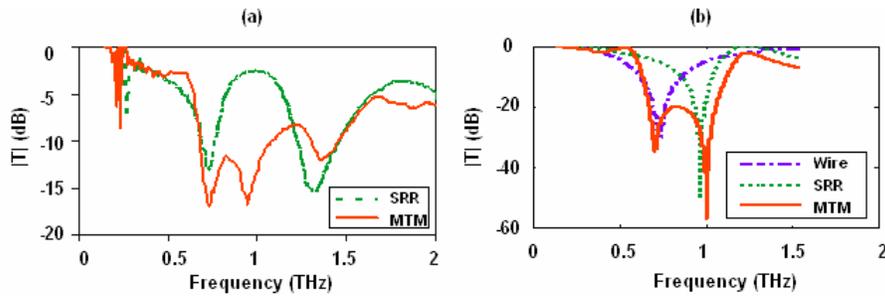
Figure 9. (a) Measured transmission spectra of SRR only (dotted line) and the composite SRR/wire structure (solid line). (b) Transmission coefficients of FDTD simulation of the wire only (dashed line), SRR only (dotted line) and the composite SRR/wire structure (solid line) of the nonplanar.

SRR and wire structures of the experimental sample ranges from 0.1 to $0.4\,\mu$m, which is much less than the modeled structure thickness ($3.9\,\mu$m). Second, the fabrication uses aluminum instead of a perfect electric conductor (PEC), which is used in the FDTD model for the MTM structures. Third, there is a misalignment between the SRRs and the wires of roughly $10\,\mu$m along the wire direction, and slightly less in the orthogonal direction for the fabricated composite structure. Fourth, Mylar is used as the substrate instead of free space in the simulation. Lastly, the model assumes semi-infinitely periodic structures, whereas the experimental results are obtained for finite periodic structures.

FDTD simulations were conducted to further explain these differences. It was found that when the thickness of the patterns is smaller, besides improving the transmissions, the pass bands also slightly shift down, as seen in the experiments. With respect to the materials, when aluminum is used for the modeled structures in the FDTD simulations, the bands of the structures shift down and become narrower, similar to the results of the experiments. It was found, however, that the misalignment is not that significant if the value is less than $10\,\mu$m. The other major factor is the Mylar film on which our structures are deposited. When it is incorporated into the computational simulations, the transmission location is shifted down and the width of the passband is reduced, agreeing more closely with the experimental results. The results of the parametric studies are shown in Fig. 10.
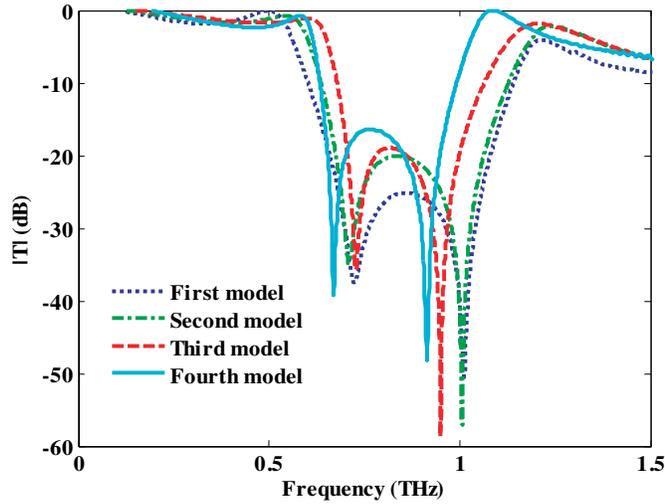
Figure 10. Simulated transmission spectra of SRR/wire structures. The parameters are thickness, structure material, misalignment, and substrate. First model: thickness 11.7 m, PEC material, no misalignment, on free space (dotted line). Second model: thickness $3.9\,\mu$m, PEC material, no misalignment, on free space (dash-dot line). Third model: thickness $3.9\,\mu$m, AL material, misalignment $7.8\,\mu$m, on free space (dashed line). Fourth model: thickness $3.9\,\mu$m, AL material, misalignment $7.8\,\mu$m, on Mylar substrate (solid line).

5. CONCLUSION

We found the broad and strong resonance of an SRR at a high frequency based on the polarization conversion theory. The orientation is set when the plane of the symmetric conventional SRR is rotated by 90, while its axis is fixed. Combining the SRRs with an array of discontinuous wires, we are able to create a NIR passband approximately two to three times higher than those of the previously known SRR/wire structures, maintaining the same dimensions. The new SRR/wire structure can produce a broad NIR passband - nearly two and a half times larger than those of the primary models. The double size structure will considerably ease the fabrication procedure when we are dealing with a very small scale at a high frequency regime. Metamaterials based on one of the models which exhibit a broad transmission band at THz frequencies are fabricated. The position and the shape of the pass band of the actual device agree relatively well with that predicted by the model.

REFERENCES

1. Woodward, R. M., "Terahertz technology in homeland security and defense," *Proc. SPIE*, Vol. 5781, 22–31, 2005.

2. Federici, J. F., D. Gary, R. Barat, and D. Zimdars, "THz standoff detection and imaging of explosives and weapons," *Proc. SPIE*, Vol. 5781, 75–84, 2005.

3. Podolskiy, V. A. and E. E. Narimanov, "Strongly anisotropic waveguide as a nonmagnetic left-handed system," *Phys. Rev. B*, Vol. 71, No. 20, 201101, 2005.

4. Katsarakis, N., T. Koschny, M. Kafesaki, E. N. Economou, and C. M. Soukoulis, "Electric coupling to the magnetic resonance of split ring resonators," *Appl. Phys. Lett.*, Vol. 84, No. 15, 2943–2945, 2004.

5. Pendry, J. B., A. J. Holden, D. J. Robbins, and W. J. Stewart, "Magnetism from conductors and enhanced nonlinear phenomena," *IEEE Trans. Microwave Theory Tech.*, Vol. 47, No. 11, 2075–2084, 1999.

6. Markos, P. and C. M. Soukoulis, "Numerical studies of left-handed materials and arrays of split ring resonators," *Phys. Rev. E*, Vol. 65, No. 3, 036622, 2002.

7. Marqués, R., F. Medina, and R. Rafii-El-Idrissi, "Role of bianisotropy in negative permeability and left-handed metamaterials," *Phys. Rev. B*, Vol. 65, No. 14, 144440, 2002.

8. Gay-Balmaz, P., and O. J. F. Martin, "Electromagnetic resonances in individual and coupled split-ring resonators," *J. Appl. Phys.*, Vol. 92, No. 5, 2929–2936, 2002.

9. Moss, C. D., T. M. Grzegorczyk, Y. Zhang, and J. A. Kong, "Numerical studies of left handed metamaterials," *PIER*, Vol. 35, 316–333, 2002.

10. Ziolkowski, R. W., "Design, fabrication, and testing of double negative metamaterials," *IEEE Trans. Antennas and Propagat.*, Vo. 51, No. 7, 1516–1529, 2003.

11. Kafesaki, M., T. Koschny, R. S. Penciu, T. F. Gundogdu, E. N. Economou, and C. M. Soukoulis, "Left-handed metamaterials: detailed numerical studies of the transmission properties," *J. Opt. A: Pure Appl. Opt.*, Vol. 7, S12–S22, 2005.

12. García-Garca, J., F. Martín, J. D. Baena, Marqués, and R. L. Jelinek, "On the resonances and polarizabilities of split ring resonators," *J. Appl. Phys.*, Vol. 98, No. 3, 033103, 2005.

13. Koschny, Th., L. Zhang, and C. M.Soukoulis, "Isotropic three-

dimensional left-handed metamaterials," *Phys. Rev. B*, Vol. 71, No. 12, 121103, 2005.

14. Enrich, C., M. Wegener, S. Linden, S. Burger, L. Zschiedrich, F. Schmidt, J. F. Zhou, Th. Koschny, and C. M. Soukoulis, "Magnetic metamaterials at telecommunication and visible frequencies," *Phys. Rev. Lett.*, Vol. 95, No. 20, 203901, 2005.

15. Islam, M. N., C. E. Soccolich, J. P. Gordon, and U. C. Paek, "Soliton intensity-dependent polarization rotation," *Opt. Lett.*, Vol. 15, No. 1, 21–23, 1990.

16. Gustavsson, M., "Analysis of polarization independent optical amplifiers and filters based," *IEEE J. Quantum Electron.*, Vol. 29, 1168–1178, 1993.

17. Derov, J. S., B. Turchinetz, E. E. Crisman, A. J. Drehman, and R. Wing, "Negative index metamaterial for selective angular separation of microwaves by polarization," *IEEE Ant. and Prop. Society Sym.*, Vol. 4, 2004.

18. Ozbay, E., K. Aydin, E. Cubukcu, and M. Bayindir, "Transmission and reflection properties of composite double negative metamaterials in free space," *IEEE Trans. Antennas Propagat.*, Vol. 51, No. 10, 2592–2595, 2003.

19. Koschny, T., M. Kafesaki, E. N. Economou, and C. M. Soukoulis, "Effective medium theory of left-handed materials," *Phys. Rev. Lett.*, Vol. 93, No. 10, 107402, 2004.

20. Katsarakis, N., T. Koschny, M. Kafesaki, E. N. Economou, E. Ozbay, and C. M. Soukoulis, "Left- and right-handed transmission peaks near the magnetic resonance frequency in composite metamaterials," *Phys. Rev. B*, Vol. 70, No. 20, 201101, 2004.

21. Shelby, R. A., D. R. Smith, and S. Schultz, "Experimental verification of a negative index of refraction," *Science*, Vol. 292, No. 5514, 77–79, 2001.